Journal of Thermal Analysis and Calorimetry (2022) 147:3453–3468
https://doi.org/10.1007/s10973-021-10586-9

Heat and mass transfer analysis of nanofluid flow over swirling cylinder with Cattaneo–Christov heat flux

P. Sudarsana Reddy[1] · P. Sreedevi[1] · Ali J. Chamkha[2,3]

Received: 1 July 2020 / Accepted: 12 January 2021 / Published online: 23 March 2021

Abstract
Single-phase nanofluid heat and mass transfer futures over swirling cylinder with the impact of Cattaneo–Christov heat flux and slip effects is studied in this analysis. The effects thermophoresis, thermal radiation, Brownian motion and chemical reaction are also considered and the motion of the fluid is because of the torsional motion of the cylinder and these parameters. Suitable similarity transformations are implemented to simplify the fluid equations from partial differential equations to ordinary differential equations. The most powerful finite element technique is applied to solve the subsequent equations along with boundary conditions. Variations in the scatterings of swirling velocity, axial velocity, concentration and temperature with several pertinent parameters are portrayed through plots. Nusselt number, both components of skin friction coefficient and Sherwood number values are also examined in detail and are revealed in tables. Temperature sketches diminish in nanofluid region with rising values of heat flux relaxation number. It is detected that the nanofluids temperature deteriorates with augmenting values of temperature slip parameter. The present numerical code is validated with existing literature.

Keywords Thermophoresis · Chemical reaction · Magnetohydrodynamics · Cattaneo–christov heat flux · Swirling cylinder · Finite element method

Abbreviations

C_f	Skin friction coefficient
k_f	Thermal conductivity of basefluid
Nt	Thermophoretic Parameter
C_∞	Ambient fluid concentration
T_w	Wall constant temperature
T	Fluid temperature
q_w	Wall heat flux
f	Dimensionless stream function
K^*	Mean absorption coefficient
Sh_x	Sherwood number
(u, v)	Velocity components in x- and y-axis
τ_w	Shear stress
M	Magnetic field parameter
B_0	Strength of Magnetic Field
(x, y)	Direction along and perpendicular to the cylinder
V	Suction parameter
C_r	Chemical reaction parameter
MHD	Magnetohydrodynamics
Nb	Brownian motion Parameter
Nu_x	Nusselt number
Re	Local Reynolds number
u_∞	Velocity of mainstream
T_∞	Ambient temperature
C	Fluid concentration
J_w	Wall mass flux
u_w	Velocity of the wall
σ^*	Stefan-Boltzmann constant
Pr	Prandtl number
R	Radiation parameter
Le	Lewis number
D_m	Diffusion coefficient
U	Composite velocity
CW	Concentration at the wall

✉ P. Sudarsana Reddy
suda1983@gmail.com

✉ Ali J. Chamkha
alichamkha@duytan.edu.vn

[1] Department of Mathematics, Rajeev Gandhi Memorial College of Engineering and Technology, Nandyal 518501, AP, India

[2] Institute of Research and Development, Duy Tan University, Da Nang 550000, Vietnam

[3] Institute of Theoretical and Applied Research (ITAR), Duy Tan University, Hanoi 100000, Vietnam

Greek symbols

α Thermal diffusivity of base fluid
μ Fluid viscosity
S Dimensionless nanoparticle volume fraction
θ Dimensionless temperature
σ Electrical conductivity
λ_1 Fluid relaxation time
B Concentration slip number
v Kinematic viscosity
ρ_p Nanoparticle mass density
η Similarity variable
λ Velocity Slip parameter
ξ Thermal slip parameter
λ_2 Thermal relaxation time
γ Thermal relaxation parameter

Subscripts

∞ Condition far away from cone surface
f Base fluid
hnf Hybrid nanofluid
nf Nanofluid

Superscripts

' Differentiation with respect to η,

Introduction

Nanofluids are exceptional fluids, having higher thermal conductivity compared to the common fluids, engendered by appending nano-sized particles in to the general liquids. The idea of nanoliquids was first familiarized in the literature by Choi et al. [1] and experimentally detected enormous rate of heat transfer after appending nanotubes in to the common fluids. By suspending magnetite nanoparticles into base fluids, we will generate magnetic nanofluids. These liquids have numerous applications in cancer therapy, optical switches, optical modulators, drug delivery, MRI scanning and optical fibers. With the help of magnetite nanoparticles, the magnetic nanofluids direct the required drug in human blood flow to annihilate tumors in human bodies. The reason is magnetic nanoparticles have the higher capacity to attack the tumor cells than the other cells [2]. Sudarsana Reddy et al. [3] presented Tiwari–Das model nanofluid flow, heat and mass transfer investigation over a vertical porous cone crammed with alumina and silver nanoparticles. Sheremet et al. [4] premeditated the impact of thermal radiation on heat transfer characteristics of unsteady nanofluid flow over an inclined enclosure with sinusoidal boundary condition.

A rotating cylinder in nanofluid flow is utilized to regulate the fluid flow and thermal transport in heat transfer mechanisms. The nanoliquid flow around a rotating cylinder has many practical applications in fluid mechanics and science and technology, such as nuclear reactor fuel rods, rotating tube–heat exchangers and many others. Munawar et al. [5] perceived the sway of entropy generation on heat transfer and flow of a three-dimensional fluid over stretchable and rotating cylinder and detected augmentation in irreversibility of fluid friction depending on curvature of the cylinder. Deylami et al. [6] presented finite volume method to analyze the flow affected by EHD actuator over circular cylinder. Sheikholeslami et al. [7, 8] studied the impact of radiation and magnetic field on heat transfer characteristics of nanofluid in a porous cavity by considering tilted elliptic cylinder inside the cavity. In this analysis, two different types of nanoparticles, namely, CuO and Fe_3O_4 are considered and analyzed its heat transfer characteristics. Selimefendigil et al. [9] professed the influence of size of the cylinder on flow and heat transfer characteristics of CuO—water-based nanofluid in a square partitioned cavity by considering rotating adiabatic cylinder at the middle of the cylinder. Akar et al. [10] perceived finite volume method to examine heat transfer and entropy generation analysis of nanofluid around a rotating cylinder and noticed intensification in the values of viscous entropy generation around the cylinder. Azam et al. [11] studied unsteady carreau nanofluid heat transfer analysis in contracting/expanding cylinder by taking zero mass flux condition, thermophoresis and Brownian motion parameters and noticed that the values of Nusselt number deteriorates with rising values of thermophoresis parameter. Dinarvand et al. [12] professed heat transfer behavior of the different nanofluids made up of titanium, alumina and copper nanoparticles through a permeable vertical cylinder and identified that copper made nanofluid has the highest rate of heat transfer compared to the other nanofluids. Nourazar et al. [13] presented thermal conductivity improvement of Silver, copper and titanium made single-phase nanofluids over a horizontal stretching cylinder and predicated that temperature of the all nanofluids worsens in the fluid region with rising values of nanoparticle volume fraction parameter. Hayat et al. [14] deliberated Buongiorno's model nanofluid mass and heat transfer characteristics through a stretched cylinder and determined that the rate of heat transfer declines with growing values of Brownian motion and thermophoresis numbers. Hussain et al. [15] discussed heat transport behavior of Sisko nanofluid flow through cylinder with the effect of Joule heating and Eckert number. Zeeshan et al. [16] pondered Buongiorno's model nanofluid mass and heat transfer characteristics over a stretching cylinder by taking Joule heating effect. Ramzan et al. [17] noticed amplification in the rate of heat transfer of nanofluid with rising values of volume fraction of nanoparticles in their study on heat transfer characteristics carbon nanotubes—water-based nanofluid flow over torsional and stretching cylinder. Javed et al. [18] deliberated Casson nanofluid flow behavior over a cylinder with heat absorption/generation and anticipated that with intensifying values of Casson parameter the temperature of the nanoliquid rises. Dogonchi et al. [19] professed heat transfer and flow analysis of Copper - water -based nanofluid flow between inner rectangular hot cylinder and external cold circular cylinder with inclined magnetic field. Usman et al. [20] noticed devaluation in the rate of heat transfer values with up surging values of thermophoresis and Brownian motion parameter in their study on mass and heat transport performance of Buongiorno's model nanofluid flow over inclined cylinder. Karbasifar et al. [21] presented the flow performance of water - alumina-based nanofluid flow over a cavity with elliptical hot centric cylinder. Dogonchi et al. [22] presented copper - water nanofluid heat transport characteristics inside horizontal circular upper half of cylinder and depicted that the Nusselt number values intensifies with rising values of nanoparticle volume fraction parameter. Nagendramma et al. [23] premeditated mass and heat transport analysis of Buongiorno's model nanoliquid flow over cylinder with double stratification. Abbas et al. [24] analyzed the behavior of three different nanofluids made up of alumina, copper and titania nanoparticles with water as base fluid over cylinder and detected that copper–water-based nanofluid has higher heat transfer rate than the other nanoliquids. Yousefi et al. [25] studied stagnation point three-dimensional hybrid nanofluid flow, made up of copper/titania hybrid nanoparticles, over circular cylinder. Selimefendigil et al. [26] demonstrated the finite volume approach to solve the mathematical formulation of nanoliquid flow over adiabatic cylinder and predicated 8.08% intensification in Nusselt number value at the maximum volume fraction of nanoparticle. Shirazi et al. [27] professed the impact of Richardson number and Rayleigh parameters on thermal conductivity improvement of water-alumina-based nanoliquid between two cylinders and noticed that heat transfer rate is enriched with growing values of volume fraction. Alizadeh et al. [28] deliberated the characteristics of Water - CuO-based magneto-hydrodynamic nanofluid flow over a cylinder and detected augmentation in rate of heat transfer with growing values of concentration of nanoparticles. Most recently, several authors [29–32] studied heat transfer performance of nanofluids over a cylinder by taking various parameters into the account.

Heat transfer is a phenomenon which takes place between two objects or within the object due to temperature difference. Two centuries back Fourier proposed Fourier's law of heat conduction to know the heat transfer characteristics. But, this law contains parabolic heat equation, which indicates that any disturbance is suddenly present initially throughout the substance. To escape from this situation, thermal relaxation time is added in the traditional Fourier's law of heat conduction by Cattaneo which permits the carriage of heat through the proliferation of thermal waves with limited speed. To attain the physical-invariant formulation, Christov amended the Cattaneo's law by adding thermal relaxation time along with Oldroyd's upper-convected derivatives. Shehzad et al. [33] perceived the sway of Cattaneo–Christov heat flux and thermal radiation on mass and heat transfer characteristics of non-Newtonian nanofluid. Raju et al. [34] discussed mass and heat transport performance of Maxwell nanofluid flow over cylinder with Cattaneo–Christov heat flux, heat sink/sink and convective boundary condition. Dogonchi et al. [35] perceived squeezing unsteady nanoliquid flow between two parallel disks with one disk is penetrable and the other is shrinking/stretching and by taking thermal relaxation parameter, heat sink/source and thermal radiation. Rauf et al. [36] studied the influence of Cattaneo–Christov heat and mass flux on unsteady three-dimensional micro-polar fluid flow over rotating disk. Li et al. [37] delivered stagnation point nanoliquid flow over shrinking/stretching sheet with Cattaneo–Christov heat flux and identified that the values of Nusselt number up surges with accumulating values of nanoparticle volume fraction parameter. Bhattacharyya et al. [38] presented carbon nanotubes heat transfer characteristics over coaxial rotating stretchable disks with thermal relaxation parameter. Kumar et al. [39] perceived flow and heat transfer of Reiner–Philippoff fluid flow over heated surface by taking Cattaneo–Christov heat flux, Ohmic heating and transverse magnetic field. Shehzad et al. [40] studied heat and mass transfer analysis of MHD Maxwell Buongiornos model nanofluid flow over rotating isolated disk with Cattaneo–Christov heat and mass fluxes. Recently several authors [41–58] studied about heat and mass transfer features of different nanofluids over various geometries by taking several parameters like, Cattaneo–Christov heat flux, magnetic field and others into the account.

Careful observation on available literature reveals that no studies have reported to analyze the impact of slip effects, Cattaneo–Christov heat flux and chemical reaction on mass and heat transport characteristics of magneto-hydrodynamic nanoliquids prepared by considering Buongiorno's model nanofluid flow over swirling cylinder. The resultant equations are solved using finite element method with Mathematica 10.0. The problem addressed in this analysis has immediate applications in generator cooling, transformer cooling, electronic cooling etc.

Mathematical analysis of the problem

Consider steady, laminar, two dimensional, MHD boundary layer heat and mass transfer of Buongiorno's model nanofluid flow through swirling cylinder with slip effects as depicted in Fig. 1. A constant external magnetic field of strength B_0 is applied normal to the plate. Cattaneo–Christov heat flux, chemical reaction and thermal radiation are also considered. Under the above assumptions, the governing

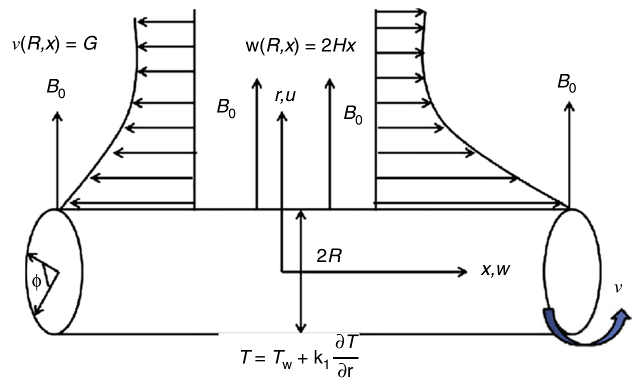

Fig. 1 Physical model and Coordinate system

equations describing the momentum, energy and concentration in the presence of chemical reaction, slip effects and thermal radiation are given by.

$$\left(\frac{\partial u}{\partial r}+\frac{\partial w}{\partial x}+\frac{u}{r}=0\right) \tag{1}$$

$$u\frac{\partial u}{\partial r}+w\frac{\partial u}{\partial x}-\frac{v^2}{r}=-\frac{1}{\rho_{\mathrm{nf}}}\frac{\partial p}{\partial r}+v_{\mathrm{nf}}\left(\frac{\partial^2 u}{\partial r^2}+\frac{1}{r}\frac{\partial u}{\partial r}+\frac{\partial^2 u}{\partial x^2}-\frac{u}{r^2}\right) \tag{2}$$

$$u\frac{\partial v}{\partial r}+w\frac{\partial v}{\partial x}+\frac{uv}{r}=v_{\mathrm{nf}}\left(\frac{\partial^2 v}{\partial r^2}+\frac{1}{r}\frac{\partial v}{\partial r}+\frac{\partial^2 v}{\partial x^2}-\frac{v}{r^2}\right)-\frac{\sigma_{\mathrm{nf}}B^2(x)}{\rho_{\mathrm{nf}}}u \tag{3}$$

$$u\frac{\partial w}{\partial r}+w\frac{\partial w}{\partial x}=-\frac{1}{\rho_{\mathrm{nf}}}\frac{\partial p}{\partial r}+v_{\mathrm{nf}}\left(\frac{\partial^2 w}{\partial r^2}+\frac{1}{r}\frac{\partial w}{\partial r}+\frac{\partial^2 w}{\partial x^2}\right)-\frac{\sigma_{\mathrm{nf}}B^2(x)}{\rho_{\mathrm{nf}}}u \tag{4}$$

$$\begin{aligned}&u\frac{\partial T}{\partial r}+w\frac{\partial T}{\partial x}+\lambda_1\left(u\frac{\partial w}{\partial r}\frac{\partial T}{\partial x}+w\frac{\partial w}{\partial x}\frac{\partial T}{\partial x}+u\frac{\partial u}{\partial r}\frac{\partial T}{\partial r}+w\frac{\partial u}{\partial x}\frac{\partial T}{\partial r}+2\mathrm{uw}\frac{\partial^2 T}{\partial x\partial r}+u^2\frac{\partial^2 T}{\partial r^2}+w^2\frac{\partial^2 T}{\partial x^2}\right)\\&=\frac{k_{\mathrm{nf}}}{\left(\rho C_p\right)_{\mathrm{nf}}}\left(\frac{\partial^2 T}{\partial r^2}+\frac{1}{r}\frac{\partial T}{\partial r}+\frac{\partial^2 T}{\partial x^2}\right)+\tau\left[D_{\mathrm{B}}\left(\frac{\partial T}{\partial r}\frac{\partial C}{\partial r}+\frac{\partial T}{\partial x}\frac{\partial C}{\partial x}\right)\right]+\frac{\tau D_{\mathrm{T}}}{T_\infty}\left[\left(\frac{\partial T}{\partial r}\right)^2+\left(\frac{\partial T}{\partial x}\right)^2\right]-\frac{1}{\left(\rho C_p\right)_{\mathrm{nf}}}\frac{\partial q_{\mathrm{r}}}{\partial y}\end{aligned} \tag{5}$$

$$\begin{aligned}u\frac{\partial C}{\partial r}+w\frac{\partial C}{\partial x}&=D_{\mathrm{B}}\left(\frac{\partial^2 C}{\partial r^2}+\frac{1}{r}\frac{\partial C}{\partial r}+\frac{\partial^2 C}{\partial x^2}\right)\\&+\frac{D_{\mathrm{T}}}{T_\infty}\left[\frac{\partial^2 T}{\partial r^2}+\frac{1}{r}\frac{\partial T}{\partial r}+\frac{\partial^2 T}{\partial x^2}\right]-C_1\left(C-C_\infty\right)\end{aligned} \tag{6}$$

The following physical boundary conditions are

$$\begin{aligned}&u=u_{\mathrm{w}},v=G,w=2\mathrm{Hx}\,L\frac{\partial w}{\partial r},T=T_{\mathrm{w}}+k_1\frac{\partial T}{\partial r},C\\&=C_{\mathrm{w}}+k_2\frac{\partial C}{\partial r},\ \mathrm{at}\,r=R.u\to u_\infty,\ T\to T_\infty,\ C\to C_\infty\ \mathrm{at}\,\mathrm{r}\to\infty\end{aligned} \tag{7}$$

The subsequent similarity transformations are presented to streamline the mathematical study of the problem

$$\begin{aligned}&\eta=\left(\frac{r}{R}\right)^2,u=-\mathrm{HR}\frac{f(\eta)}{\sqrt{\eta}},\\&v=\mathrm{Gg}(\eta),w=2\mathrm{Hx}\,f'(\eta),\theta(\eta)=\frac{T-T_\infty}{T_{\mathrm{w}}-T_\infty},\\&S(\eta)=\frac{C-C_\infty}{C_{\mathrm{w}}-C_\infty}\end{aligned} \tag{8}$$

By utilizing Rosseland estimation for radiation, the radiative heat flux q_{r} is demarcated as

$$q_{\mathrm{r}}=-\frac{4\sigma^*}{3K^*}\frac{\partial T^4}{\partial r}=-\frac{16\sigma^* T^3}{3K^*}\frac{\partial T}{\partial r} \tag{9}$$

The transformed equations are

$$\eta f'''+f''-\mathrm{Re}\left(\left(f'\right)^2-ff''\right)-Mf'=0 \tag{10}$$

$$\eta g''+g'-\frac{g}{4\eta}-\mathrm{Re}\left(\frac{fg}{2\eta}-fg'\right)-Mg=0 \tag{11}$$

$$\begin{aligned}&(1+R)\eta\theta''+\theta'+\mathrm{Pr}\,\mathrm{Re}f\theta'-\mathrm{Pr}\,\mathrm{Re}\gamma\left(f^2\theta''+ff'\theta'\right)\\&+\mathrm{Pr}\left(\mathrm{Nb}\eta\theta' S'+\mathrm{Nt}\theta'^2\right)=0\end{aligned} \tag{12}$$

$$\eta S''+S'+\mathrm{Re}LefS'+\frac{\mathrm{Nt}}{\mathrm{Nb}}\left(\theta'+\eta\theta''\right)-\mathrm{Re}C_{\mathrm{r}}LeS=0 \tag{13}$$

The associated converted boundary conditions are

$$\begin{aligned}&f(1)=V_0,f'(1)=\lambda f''(1),\\&g(1)=1,\ \theta(1)=1+\xi\theta'(1),S(1)=1+\beta S'(1).\\&f'(\infty)\to 1,\ g(\infty)\to 0,\ \theta(\infty)\to 0,\ S(\infty)\to 0.\end{aligned} \tag{14}$$

The associated non-dimensional parameters are defined as

$$\mathrm{Pr} = \frac{\nu_f c_p}{k},\ \gamma = 2\lambda_1 H,\ \lambda = \frac{2L}{R},\ M = \frac{\sigma B_0^2 R^2}{4\nu\rho},$$
$$\xi = \left(\frac{2k_1}{R}\right), \mathrm{Nt} = \frac{\tau D_T (T_w - T_\infty)}{\nu T_\infty},$$
$$\beta = \left(\frac{2k_2}{R}\right),\ \mathrm{Le} = \frac{\nu}{D_B},\ \mathrm{Re} = \frac{H\,R^2}{2\nu},\ C_r = \frac{C_1}{2H},$$
$$R = \frac{16T_\infty^3\sigma^*}{3k^* k_f},\ \mathrm{Nb} = \frac{\tau D_B (C_w - C_\infty)}{\nu},$$

The another object of this problem is to calculate skin friction coefficients along swirling and radial directions, Nusselt number and Sherwood number are given as

$$\mathrm{Re}C_{fx} = f''(1),\ \mathrm{Re}C_{fs} = 2g'(1) - g(1),\ \mathrm{Re}^{-1/2}\mathrm{Nu}_x = -(1+\gamma)\theta'(1),\ \mathrm{Re}^{1/2}\mathrm{Sh}_x = -S'(1) \tag{15}$$

where (Re) represents the local Reynolds number.

Numerical solution of the problem

The finite element method

The variational finite element process [59–62] is implemented to evaluate numerically above Eqs. (10–13) with boundary conditions (14). Compare to other numerical methods finite element method is the better method to solve both ordinary and partial differential equations numerically. The steps involved in the finite element method are as follows.

(1) Finite element discretization
The whole domain is divided into a finite number of subdomains, which is called the discretization of the domain. Each subdomain is called an element. The collection of elements is called the finite element mesh.

(2) Generation of the element equations

a. From the mesh, a typical element is isolated and the variational formulation of the given problem over the typical element is constructed.
b. An approximate solution of the variational problem is assumed, and the element equations are made by substituting this solution in the above system.
c. The element matrix, which is called stiffness matrix, is constructed by using the element interpolation functions.

(3) Assembly of element equations
The algebraic equations so obtained are assembled by imposing the interelement continuity conditions. This yields a large number of algebraic equations known as the global finite element model, which governs the whole domain.

(4) Imposition of boundary conditions
The essential and natural boundary conditions are imposed on the assembled equations.

(5) Solution of assembled equations
The assembled equations so obtained can be solved by any of the numerical techniques, namely, the Gauss elimination method, LU decomposition method, etc. An important consideration is that of the shape functions which are employed to approximate actual functions.

For the solution of system of non-linear ordinary differential Eqs. (10–13) together with boundary conditions (14), first we assume that

$$\frac{df}{d\eta} = \mathrm{h} \tag{16}$$

The Eqs. (10–13) then reduces to

$$\eta\, h'' - h' - \mathrm{Re}\left[h^2 - fh'\right] - \mathrm{Mh} = 0. \tag{17}$$

$$\eta\, g'' + g' - \frac{g}{4\eta} - \mathrm{Re}\left[\frac{fg}{2\eta} - fg'\right] - \mathrm{Mg} = 0. \tag{18}$$

$$(1+R)\eta\theta'' + \theta' + \mathrm{Pr\,Re}f\theta' - \mathrm{Pr\,Re}\gamma\left[f^2\theta'' + ff'\theta'\right] + \mathrm{Pr}[Nb\eta\theta' S' + Nt(\theta')^2] = 0 \tag{19}$$

$$\eta S'' + S' + \mathrm{ReLef}S' + \frac{\mathrm{Nt}}{\mathrm{Nb}}\left[\theta' + \eta\theta''\right] - \mathrm{ReCr\ Le}\ S = 0 \tag{20}$$

The boundary conditions take the form

$$f(1) = 0,\ h(1) = \lambda h'(1),\ \theta(1) = 1 + \xi\theta'(1),\ S(1) = 1 + \beta S'(1).$$
$$f'(\infty) \to 1,\ g(\infty) \to 0,\ \theta(\infty) \to 0,\ S(\infty) \to 0 \tag{21}$$

Variational formulation

The variational form associated with Eqs. (16–20) over a typical linear element (η_e, η_{e+1}) is given by

$$\int_{\eta_e}^{\eta_{e+1}} w_1\left(\frac{df}{d\eta} - h\right)d\eta = 0 \tag{22}$$

$$\int_{\eta_e}^{\eta_{e+1}} w_2\left(\eta h'' - h' - \mathrm{Re}\left[h^2 - fh'\right] - \mathrm{Mh}\right)\mathrm{d}\eta = 0 \tag{23}$$

$$\int_{\eta_e}^{\eta_{e+1}} w_3\left(\eta g'' + g' - \frac{g}{4\eta} - \mathrm{Re}\left[\frac{\mathrm{fg}}{2\eta} - \mathrm{fg}'\right] - \mathrm{Mg}\right)\mathrm{d}\eta = 0 \tag{24}$$

where $[K^{mn}]$ and $[r^m]$ $(m, n = 1, 2, 3, 4, 5)$ are defined as

$$K_{ij}^{11} = \int_{\eta_e}^{\eta_{e+1}} \psi_i \frac{\partial \psi_j}{\partial \eta} d\eta,\ K_{ij}^{12} = -\int_{\eta_e}^{\eta_{e+1}} \psi_i \psi_j d\eta,\ K_{ij}^{13} = K_{ij}^{14} = K_{ij}^{15} = 0.$$

$$\begin{aligned} K_{ij}^{22} = {} & \eta \int_{\eta_e}^{\eta_{e+1}} \frac{\partial \psi_i}{\partial \eta}\frac{\partial \psi_j}{\partial \eta} d\eta + \int_{\eta_e}^{\eta_{e+1}} \psi_i \frac{\partial \psi_j}{\partial \eta} d\eta - \mathrm{Re}\overline{h_1} \int_{\eta_e}^{\eta_{e+1}} \psi_i \psi_1 \psi_j d\eta \\ & + \mathrm{Re}\overline{h_2} \int_{\eta_e}^{\eta_{e+1}} \psi_i \psi_2 \psi_j d\eta + \mathrm{Re}\overline{f_1} \int_{\eta_e}^{\eta_{e+1}} \psi_i \psi_1 \frac{\partial \psi_j}{\partial \eta} d\eta - \mathrm{Re}\overline{f_2} \int_{\eta_e}^{\eta_{e+1}} \psi_i \psi_1 \frac{\partial \psi_j}{\partial \eta} d\eta, \\ & - \frac{1}{2}\tau\eta \int_{\eta_e}^{\eta_{e+1}} \psi_i \psi_j d\eta - M \int_{\eta_e}^{\eta_{e+1}} \psi_i \psi_j d\eta \end{aligned}$$

$$\int_{\eta_e}^{\eta_{e+1}} \left((1+R)\eta\theta'' + \theta' + \mathrm{Pr}\,\mathrm{Re} f\theta' - \mathrm{Pr}\,\mathrm{Re}\gamma\left[f^2\theta'' + \mathrm{ff}'\theta' + \mathrm{Pr}\left[\mathrm{Nb}\eta\theta' S' + \mathrm{Nt}\left(\theta'\right)^2\right]\right]\right)\mathrm{d}\eta = 0 \tag{25}$$

$$\int_{\eta_e}^{\eta_{e+1}} w_5\left(\eta S'' + S' + \mathrm{ReLefS}' + \frac{\mathrm{Nt}}{\mathrm{Nb}}\left[\theta' + \eta\theta''\right] - \mathrm{ReCrLe}S\right)d\eta = 0 \tag{26}$$

where w_1, w_2, w_3, w_4 and w_5 are arbitrary test functions and may be viewed as the variations in f, h, g, θ, and S, respectively.

Finite element formulation

The finite element model may be obtained from above equations by substituting finite-element approximations of the form

$$f = \sum_{j=1}^{2} f_j\psi_j,\ h = \sum_{j=1}^{2} h_j\psi_j,\ g = \sum_{j=1}^{2} g_j\psi_j,\ \theta = \sum_{j=1}^{2} \theta_j\psi_j,\ S = \sum_{j=1}^{2} S_j\psi_j \tag{27}$$

with $\mathrm{w}_1 = \mathrm{w}_2 = \mathrm{w}_3 = \mathrm{w}_4 = \mathrm{w}_5 = \psi_i, (i = 1, 2, 3)$.

Where ψ_i are the shape functions for a typical element $(\eta_e,\ \eta_{e+1})$ and are defined as

$$\begin{aligned} \psi_1^e &= \frac{(\eta_{e+1} + \eta_e - 2\eta)(\eta_{e+1} - \eta)}{(\eta_{e+1} - \eta_e)^2},\ \psi_2^e = \frac{4(\eta - \eta_e)(\eta_{e+1} - \eta)}{(\eta_{e+1} - \eta_e)^2}, \\ \psi_3^e &= \frac{(\eta_{e+1} + \eta_e - 2\eta)(\eta - \eta_e)}{(\eta_{e+1} - \eta_e)^2},\ \eta_e \le \eta \le \eta_{e+1} \end{aligned} \tag{28}$$

The finite element model of the equations thus formed is given by

$$\begin{bmatrix} [K^{11}] & [K^{12}] & [K^{13}] & [K^{14}] & [K^{15}] \\ [K^{21}] & [K^{22}] & [K^{23}] & [K^{24}] & [K^{25}] \\ [K^{31}] & [K^{32}] & [K^{33}] & [K^{34}] & [K^{35}] \\ [K^{41}] & [K^{42}] & [K^{43}] & [K^{44}] & [K^{45}] \\ [K^{51}] & [K^{52}] & [K^{53}] & [K^{54}] & [K^{55}] \end{bmatrix} \begin{bmatrix} f \\ h \\ g \\ \theta \\ S \end{bmatrix} = \begin{bmatrix} \{r^1\} \\ \{r^2\} \\ \{r^3\} \\ \{r^4\} \\ \{r^5\} \end{bmatrix}$$

$$\mathrm{K_{ij}}^{23} = \mathrm{K_{ij}}^{24} = \mathrm{K_{ij}}^{25} = 0.$$

$$\mathrm{K}_{ij}^{31} = 0,\ \mathrm{K}_{ij}^{32} = 0,$$

$$\begin{aligned} K_{ij}^{33} = {} & \eta \int_{\eta_e}^{\eta_{e+1}} \frac{\partial \psi_i}{\partial \eta}\frac{\partial \psi_j}{\partial \eta} d\eta + \int_{\eta_e}^{\eta_{e+1}} \psi_i \frac{\partial \psi_j}{\partial \eta} d\eta - \frac{1}{4\eta} \int_{\eta_e}^{\eta_{e+1}} \psi_i \psi_j d\eta \\ & - \frac{\mathrm{Re}}{2\eta}\overline{f_1} \int_{\eta_e}^{\eta_{e+1}} \psi_i \psi_1 \psi_j d\eta - \frac{\mathrm{Re}}{2\eta}\overline{f_2} \int_{\eta_e}^{\eta_{e+1}} \psi_i \psi_1 \psi_j d\eta + \mathrm{Re}\overline{f_1} \int_{\eta_e}^{\eta_{e+1}} \psi_i \psi_1 \frac{\partial \psi_j}{\partial \eta} d\eta, \\ & + \mathrm{Re}\overline{f_1} \int_{\eta_e}^{\eta_{e+1}} \psi_i \psi_1 \frac{\partial \psi_j}{\partial \eta} d\eta - M \int_{\eta_e}^{\eta_{e+1}} \psi_i \psi_j d\eta \end{aligned}$$

$$K_{ij}^{34} = 0, K_{ij}^{35} = 0$$

$$K_{ij}^{41} = 0, K_{ij}^{42} = 0, K_{ij}^{43} = 0,$$

$$\begin{aligned} K_{ij}^{44} = {} & \eta(1+R) \int_{\eta_e}^{\eta_{e+1}} \frac{\partial \psi_i}{\partial \eta}\frac{\partial \psi_j}{\partial \eta} d\eta + \int_{\eta_e}^{\eta_{e+1}} \psi_i \frac{\partial \psi_j}{\partial \eta} d\eta + \mathrm{Pr}\,\mathrm{Re}\overline{f_1} \int_{\eta_e}^{\eta_{e+1}} \psi_i \psi_1 \frac{\partial \psi_j}{\partial \eta} d\eta \\ & + \mathrm{Pr}\,\mathrm{Re}\overline{f_2} \int_{\eta_e}^{\eta_{e+1}} \psi_i \psi_2 \frac{\partial \psi_j}{\partial \eta} d\eta - \mathrm{Pr}\,\mathrm{Re}\gamma \int_{\eta_e}^{\eta_{e+1}} \frac{\partial \psi_i}{\partial \eta}^2 \frac{\partial \psi_i}{\partial \eta}\frac{\partial \psi_j}{\partial \eta} d\eta \\ & - \mathrm{Pr}\,\mathrm{Re}\gamma \int_{\eta_e}^{\eta_{e+1}} \psi_i \left(\frac{\partial \psi_j}{\partial \eta}\right) \psi_i \left(\frac{\partial \psi_j}{\partial \eta}\right) d\eta + \mathrm{Pr}\,\mathrm{Nb}\eta\overline{s_1} \int_{\eta_e}^{\eta_{e+1}} \psi_i \psi_1 \frac{\partial \psi_j}{\partial \eta} d\eta \\ & + \mathrm{Pr}\,\mathrm{Nb}\eta\overline{s_2} \int_{\eta_e}^{\eta_{e+1}} \psi_i \psi_2 \frac{\partial \psi_j}{\partial \eta} d\eta + \mathrm{Pr}\,Nt\overline{\theta_1} \int_{\eta_e}^{\eta_{e+1}} \frac{\partial \psi_i}{\partial \eta}\frac{\partial \psi_j}{\partial \eta} d\eta + \mathrm{Pr}\,\mathrm{Nt}\overline{\theta_2} \int_{\eta_e}^{\eta_{e+1}} \frac{\partial \psi_i}{\partial \eta}\frac{\partial \psi_j}{\partial \eta} d\eta \end{aligned}$$

$$\mathrm{K}_{ij}^{45} = 0.$$

$$K_{ij}^{51} = 0, K_{ij}^{52} = 0, K_{ij}^{53} = 0.$$

$$K_{ij}^{54} = \frac{\mathrm{Nt}}{\mathrm{Nb}} \int_{\eta_e}^{\eta_{e+1}} \psi_i \frac{\partial \psi_j}{\partial \eta} d\eta + \eta \frac{\mathrm{Nt}}{\mathrm{Nb}} \int_{\eta_e}^{\eta_{e+1}} \frac{\partial \psi_i}{\partial \eta} \frac{\partial \psi_j}{\partial \eta} d\eta,$$

$$K_{ij}^{55} = \eta \int_{\eta_e}^{\eta_{e+1}} \frac{\partial \psi_i}{\partial \eta} \frac{\partial \psi_j}{\partial \eta} d\eta + \int_{\eta_e}^{\eta_{e+1}} \psi_i \frac{\partial \psi_j}{\partial \eta} d\eta + \mathrm{ReLe}\overline{f_1} \int_{\eta_e}^{\eta_{e+1}} \psi_i \frac{\partial \psi_j}{\partial \eta} d\eta + \mathrm{ReLe}\overline{f_2} \int_{\eta_e}^{\eta_{e+1}} \psi_i \frac{\partial \psi_j}{\partial \eta} d\eta - \mathrm{ReCr\ Le} \int_{\eta_e}^{\eta_{e+1}} \psi_i \psi_j d\eta.$$

$$r_i^2 = 0 \ , \quad r_i^2 = -\left(\psi_i \frac{d\psi_i}{d\eta}\right)_{\eta_e}^{\eta_{e+1}} \ , \quad r_i^3 = -\left(\psi_i \frac{d\psi_i}{d\eta}\right)_{\eta_e}^{\eta_{e+1}} \ ,$$

$$r_i^4 = -\left(\psi_i \frac{d\psi_i}{d\eta}\right)_{\eta_e}^{\eta_{e+1}}.$$

$$r_i^5 = -\left(\psi_i \frac{d\psi_i}{d\eta}\right)_{\eta_e}^{\eta_{e+1}}.$$

Results and discussion

The impact of several parameters on the profiles of velocity $\left(f'(\eta), g(\eta)\right)$, temperature scatterings $(\theta(\eta))$ and concentration sketches $(S(\eta))$ is discussed in this section, and the corresponding graphical profiles are presented in Figs. 2–28. The results are corroborated with Alebraheem et al. [63] which are shown in Table 1 and found that the results are in good agreement. The values of skin friction coefficients $\left(f''(1), g'(1)\right)$, Nusselt number $\left(-\theta'(1)\right)$ and Sherwood number $\left(-S'(1)\right)$ for different values of key parameters are shown in Tables 2 and 3.

Figures 2–4 illustrate the swirling velocity, axial velocity and temperature sketches for variant values of magnetic number (M). It is noticed from Figs. 2 and 3 that the rise in magnetic parameter (M) depreciates both swirling and axial velocities of the nanofluid. However, the nanofluids temperature augments with boosting values of magnetic field parameter (M) as depicted in Fig. 4. This is because the inclusion of magnetic field into the fluid creates Lorentz force which opposes nanoliquids velocity results deterioration in the thickness of the hydrodynamic boundary layer. Fluid has to perform extra work to overcome this drag force causes augmentation in the temperature of the fluid.

Sketches of swirling velocity, axial velocity, temperature and concentration for dissimilar values of Reynolds number (Re) are portrayed in Figs. 5–8. Both swirling and axial velocities, temperature and concentration sketches worsen with intensifying values of Reynolds number (Re). The reason is higher the values of Reynolds number creates more inertial effect causes decrement in the viscosity of the fluid results deterioration in the thickness of all boundary layers.

Figures 9 and 10 portray the sway of Prandtl number (Pr) on thermal and solutal boundary layers. With up surging values of (Pr) the temperature sketches of the nanoliquid degenerates, whereas concentration sketches of the nanoliquid intensifies with accumulating values of (Pr). It is professed from Fig. 11 that the temperature sketches decelerate with growing values of thermal relaxation parameter (γ). Nevertheless, the concentration sketches augmented with rising values of (γ) and delineated in Fig. 12.

Figures 13 and 14 are displayed to comprehend the Brownian motion parameter (Nb) impression on temperature and concentration distribution. It is perceived that temperature distribution extends with increasing values of (Nb) as shown in Fig. 13, whereas the concentration distribution depreciates with rising values of (Nb). Figure 15 exemplifies the consequence of thermophoresis parameter (Nt) on temperature distribution. It is cognized that temperature upsurges with an enhanced values of (Nt).

The consequences of radiation parameter (R) on temperature and concentration dispersal are summarized in Figs. 16 and 17, and it is authenticated that temperature dispersal is heighten with escalated values of (R), whereas the concentration dispersal is abatement as values of R optimizes.

The yield of velocity slip parameter (λ) on sketches of swirling and axial velocity, temperature and concentration of Cattaneo–Christov nanofluid is characterized in Figs. 18–21. The swirling velocity dispersal developed throughout the regime as the values of (λ) step-up, whereas the axial velocity dispersal depletion with upgrade values of (λ). The thermal dispersal and diffusion dispersal waning with improved values of (λ).

Figures 22 and 23 elucidate the yield of thermal slip parameter (ξ) on thermal and solutal boundary layers of nanofluid. With the escalating values of (ξ) the temperature and concentration sketches deteriorate. The sketches of concentration truncate with the higher values of concentration slip parameter (β) in entire fluid regime and are portrayed in Fig. 24.

The yield of chemical reaction parameter (Cr) on concentration sketches is characterized in Fig. 25. It is remarked that the diffusion boundary layer thickness is compressible with access values of (Cr). Figures 26, 27 and 28 are authenticated to describe the impact of suction/injection parameter (V0) on swirling and axial velocity components and temperature profile. It is revealed that spreading values of

(V0) subsidence the swirling and axial velocity components, temperature fields.

Table 2 is incorporate of numerically calculated values of skin friction coefficient, Nusselt number and Sherwood number for M, Re, Pr, γ, R, V0. With the accumulated values of (M) and (R), there is an enhancement in the magnitudes of both skin friction components and Sherwood number, whereas Nusselt number diminishes. It is inspected that for boosted values of (Pr) and (γ) magnitude of rate of velocity and rate of concentration reduces. However, the magnitude of heat transfer rate upsurges as the values of (Pr) and (γ) rises. It is estimated that from this table all the values of skin friction coefficient, Nusselt number and Sherwood number develops as (Re) values rises. The magnitude of all $\left(f''(1)\right)$, $\left(g'(1)\right)$ & $\left(-\theta'(1)\right)$ values elaborates as (V0) values optimizes, nevertheless, Sherwood number worsen with improving values of (V0).

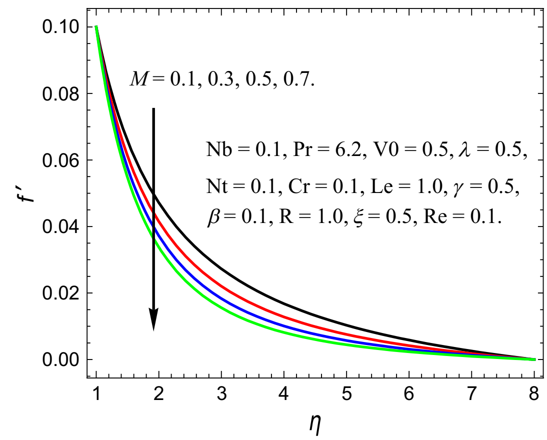

Fig. 2 The influence of (M) on f'

The sway of Nb, Nt, λ, ξ, β&Cr on skin friction coefficient, Nusselt number and Sherwood number is characterized in Table 3. All the values of $\left(f''(1)\right)$, $\left(g'(1)\right)$, $\left(-\theta'(1)\right)$ & $\left(-S'(1)\right)$ truncates in entire regime with up surging values of (Nt), whereas, all the values amplifies with upturn values of (λ). It is perceived that for developed values of (Nb), (β) and (Cr), the rates of velocity and rates of heat transfer are both declines in the fluid region. However, the rates of mass transfer rise for (Nb), (Cr) and depreciate with improving values of (β). With improving values of (ξ), the values of $\left(f''(1)\right)$, $\left(g'(1)\right)$, $\left(-S'(1)\right)$ are hiked, whereas values of $\left(-\theta'(1)\right)$ depletion in the fluid regime.

Table 1 Comparison of $\left(\mathrm{Re}C_{fx} \& \mathrm{Re}C_{fs}\right)$ for $V0 = 0, Cr = 0, \lambda = 0, \xi = 0, \beta = 0,$ $Pr = 0.5, Nt = 0.1, Nb = 0.3$ $, Le = 1.0$

Parameter			Alebraheem et al. [63]		Present study	
M	β	Re	$\mathrm{Re}C_{fx}$	$\mathrm{Re}C_{fs}$	$\mathrm{Re}C_{fx}$	$\mathrm{Re}C_{fs}$
0.2	3.0	0.2	− 1.1918	− 3.1565	− 1.1922	− 3.1568
0.3			− 1.2564	− 3.3343	− 1.2568	− 3.3347
0.4			− 1.3164	− 3.4894	− 1.3169	− 3.4898
	4.0		− 1.3032	− 3.6519	− 1.3035	− 3.6514
	5.0		− 1.1685	− 3.1191	− 1.1689	− 3.1196
	6.0		− 1.1216	− 2.9505	− 1.1219	− 2.9508
		0.2	− 0.8876	− 3.1650	− 0.8871	− 3.1658
		0.4	− 1.0669	− 3.2318	− 1.0665	− 3.2314
		0.6	− 1.2143	− 3.2972	− 1.2148	− 3.2976

Table 2 The sway of pertinent parameters entered into the problem on skin friction coefficient $(f''(1)\&g'(1))$, local Nusselt number $(-\theta'(1))$ and local Sherwood number $(-S\prime(1))$

Parameters						$f''(1)$	$g'(1)$	$-\theta'(1)$	$-S'(1)$
M	Re	Pr	γ	R	V0	– 0.09745	– 4.40207	1.15648	0.93127
0.1	1.0	2.0	0.2	0.5	0.5	– 0.11382	– 4.66511	1.15166	0.93201
0.3	1.0	2.0	0.2	0.5	0.5	– 0.12744	– 4.89473	1.14799	0.93258
0.5	1.0	2.0	0.2	0.5	0.5	– 0.13924	– 5.10009	1.14508	0.93303
0.7	1.0	2.0	0.2	0.5	0.5	– 0.06090	– 2.75129	1.15648	0.93127
0.1	1.0	2.0	0.2	0.5	0.5	– 0.06592	– 2.86606	1.27839	0.98044
0.1	1.2	2.0	0.2	0.5	0.5	– 0.07103	– 2.98190	1.39760	1.02614
0.1	1.4	2.0	0.2	0.5	0.5	– 0.07623	– 3.09873	1.51310	1.06927
0.1	1.6	2.0	0.2	0.5	0.5	– 0.09745	– 4.40207	1.61518	1.80389
0.1	1.0	2.2	0.2	0.5	0.5	– 0.09732	– 4.40205	1.46499	0.77873
0.1	1.0	2.4	0.2	0.5	0.5	– 0.09723	– 4.40196	1.51399	0.75379
0.1	1.0	2.6	0.2	0.5	0.5	– 0.09654	– 4.40178	1.60938	0.72171
0.1	1.0	2.8	0.2	0.5	0.5	– 0.09645	– 4.40107	1.04834	0.68124
0.1	1.0	2.0	0.5	0.5	0.5	– 0.09645	– 4.40206	1.13215	0.94004
0.1	1.0	2.0	1.0	0.5	0.5	– 0.09542	– 4.40204	1.23743	0.88745
0.1	1.0	2.0	1.5	0.5	0.5	– 0.09454	– 4.40123	1.37348	0.81823
0.1	1.0	2.0	2.0	0.5	0.5	– 0.09245	– 4.40007	1.55929	0.80920
0.1	1.0	2.0	0.2	0.3	0.5	– 0.09765	– 4.40312	1.15648	0.93127
0.1	1.0	2.0	0.2	0.5	0.5	– 0.09845	– 4.40354	1.07334	0.97271
0.1	1.0	2.0	0.2	0.7	0.5	– 0.09865	– 4.40425	1.04652	1.00646
0.1	1.0	2.0	0.2	0.9	0.5	– 0.08540	– 4.07047	0.92644	0.95219
0.1	1.0	2.0	0.2	0.5	0.3	– 0.09745	– 4..40207	1.15648	0.93127
0.1	1.0	2.0	0.2	0.5	0.5	– 0.11054	– 4.74511	1.41401	0.89161
0.1	1.0	2.0	0.2	0.5	0.7	– 0.12461	– 5.09782	1.70068	0.83501
0.1	1.0	2.0	0.2	0.5	0.9	– 0.19745	– 5.40207	1.85648	0.73127

Table 3 The sway of pertinent parameter entered into the problem on skin friction coefficient $(f''(1), g'(1))$, local Nusselt number $(-\theta'(1))$ and local Sherwood number $(-S'(1))$.

Parameters						$f(1)$	$g'(1)$	$-\theta'(1)$	$-s'(1)$
Nb	Nt	λ	ξ	β	Cr				
0.2	0.1	0.1	0.5	0.1	0.5	– 0.09745	– 4.40207	0.93964	1.06894
0.4	0.1	0.1	0.5	0.1	0.5	– 0.09743	– 4.40206	0.86091	1.09593
0.6	0.1	0.1	0.5	0.1	0.5	– 0.09732	– 4.40196	0.78540	1.10460
0.8	0.1	0.1	0.5	0.1	0.5	– 0.09721	– 4.40158	0.71349	1.10867
0.1	0.1	0.1	0.5	0.1	0.5	– 0.09745	– 4.40207	1.15648	0.93127
0.1	0.3	0.1	0.5	0.1	0.5	– 0.09743	– 4.40206	1.07278	0.70977
0.1	0.5	0.1	0.5	0.1	0.5	– 0.09625	– 4.40125	0.98852	0.64996
0.1	0.7	0.1	0.5	0.1	0.5	– 0.09545	– 4.40114	0.90454	0.45976
0.1	0.1	1.2	0.5	0.1	0.5	– 0.62508	– 4.64674	1.35870	0.31048
0.1	0.1	1.4	0.5	0.1	0.5	– 1.50698	– 4.89494	1.53904	0.90417
0.1	0.1	1.6	0.5	0.1	0.5	– 2.57374	– 5.10678	1.67762	0.90949
0.1	0.1	1.8	0.5	0.1	0.5	– 3.79225	– 5.29489	1.79150	0.92125
0.1	0.1	0.1	0.5	0.1	0.5	– 0.09745	– 4.40207	1.15648	0.93127
0.1	0.1	0.1	0.7	0.1	0.5	– 0.09746	– 4.41206	1.10400	0.94726
0.1	0.1	0.1	0.9	0.1	0.5	– 0.09825	– 4.42205	0.94440	0.96064
0.1	0.1	0.1	1.0	0.1	0.5	– 0.09954	– 4.44125	0.90273	0.96654
0.1	0.1	0.1	0.5	0.1	0.5	– 0.09745	– 4.40207	1.15648	0.93127
0.1	0.1	0.1	0.5	0.3	0.5	– 0.09746	– 4.40302	1.16671	0.75862
0.1	0.1	0.1	0.5	0.5	0.5	– 0.09758	– 4.40523	1.17374	0.63997
0.1	0.1	0.1	0.5	0.7	0.5	– 0.09854	– 4.40687	1.17888	0.55341
0.1	0.1	0.1	0.5	0.1	0.5	– 0.09745	– 4.40207	1.15648	0.93127
0.1	0.1	0.1	0.5	0.1	0.7	– 0.09654	– 4.40105	1.15393	1.04678
0.1	0.1	0.1	0.5	0.1	0.9	– 0.09524	– 4.40104	1.15202	1.14495
0.1	0.1	0.1	0.5	0.1	1.0	– 0.09458	– 4.40098	1.15123	1.18916

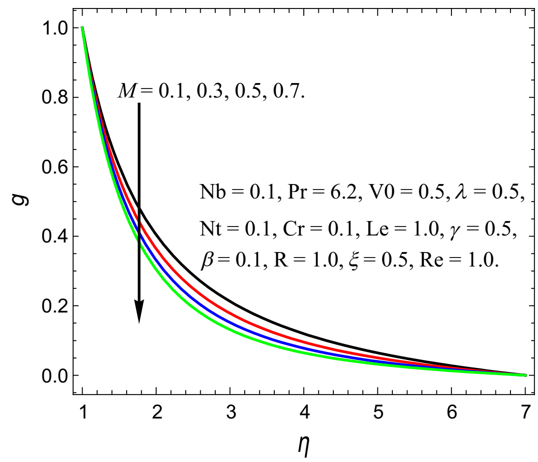

Fig. 3 The influence of (M) on g

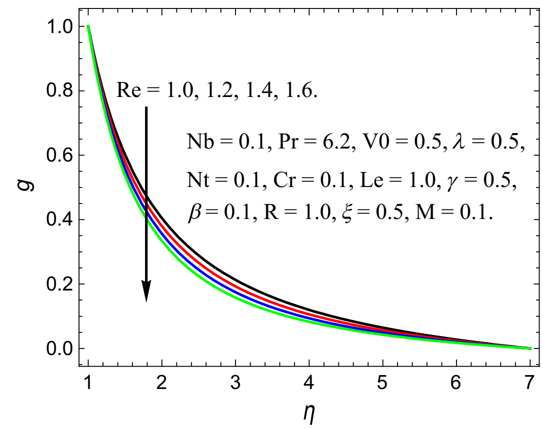

Fig. 6 The influence of (Re) on g

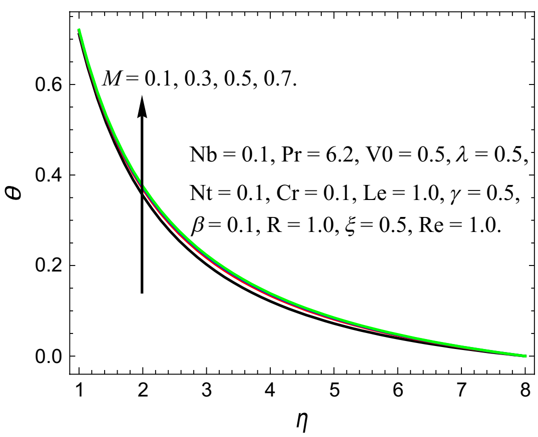

Fig. 4 The influence of (M) on θ

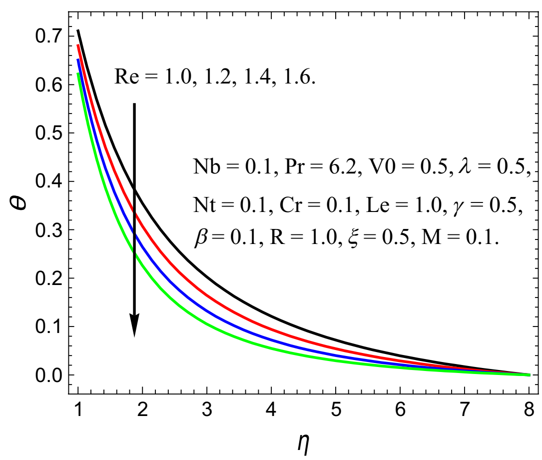

Fig. 7 The influence of (Re) on θ

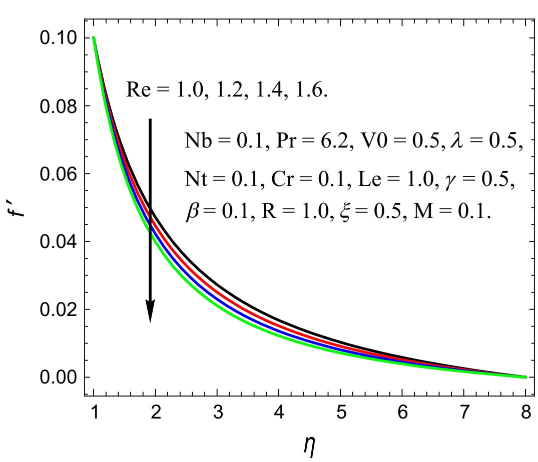

Fig. 5 The influence of (Re) on f'

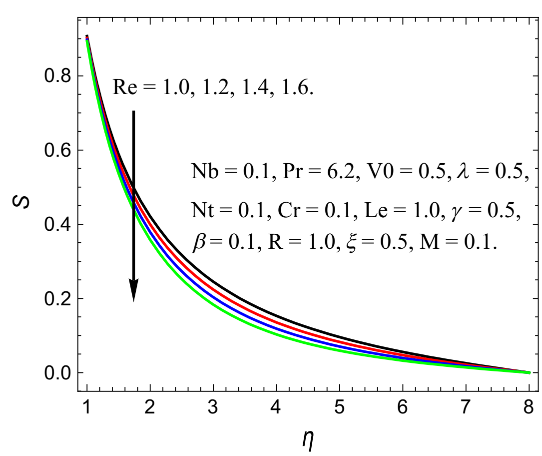

Fig. 8 The influence of (Re) on S

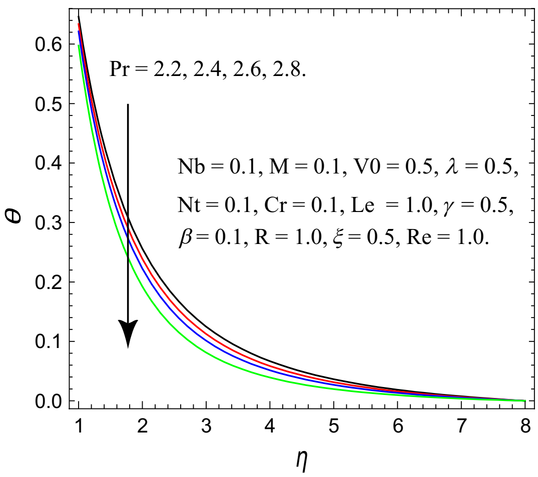

Fig. 9 The influence of (Pr) on θ

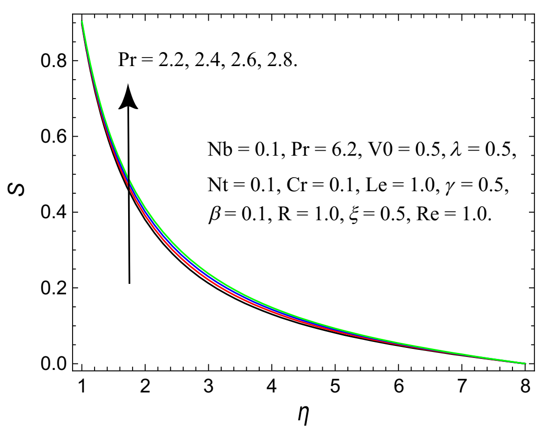

Fig. 10 The influence of (Pr) on S

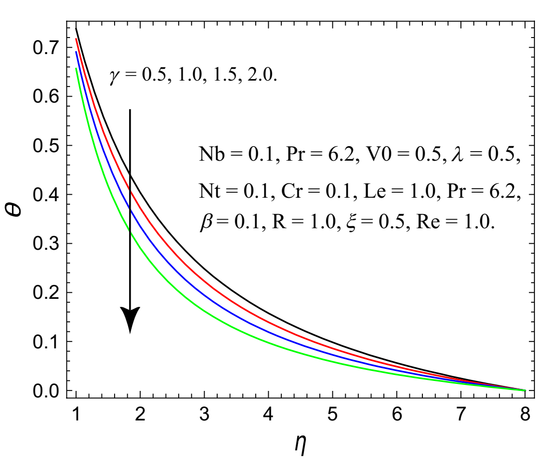

Fig. 11 The influence of (γ) on θ

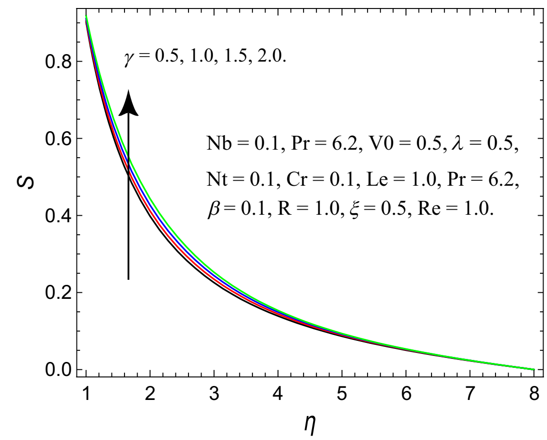

Fig. 12 The influence of (γ) on S

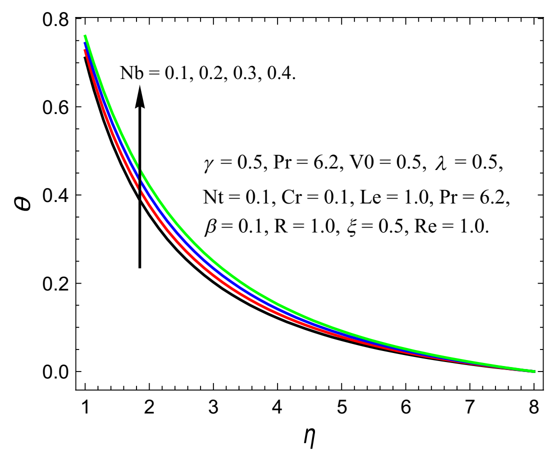

Fig. 13 The influence of (Nb) on θ

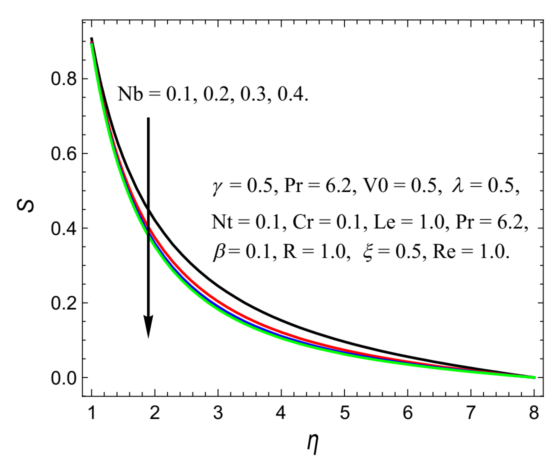

Fig. 14 The influence of (Nb) on S

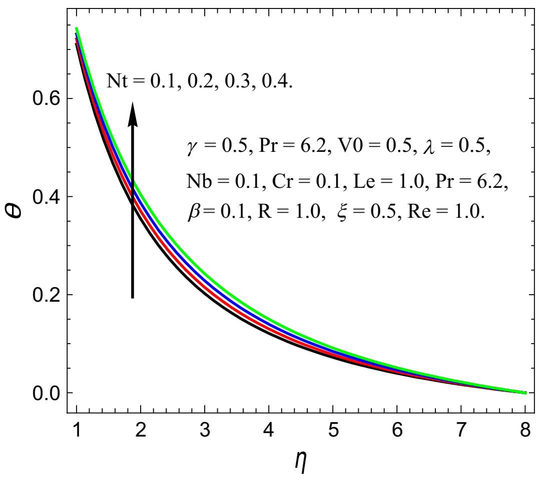

Fig. 15 The influence of (Nt) on θ

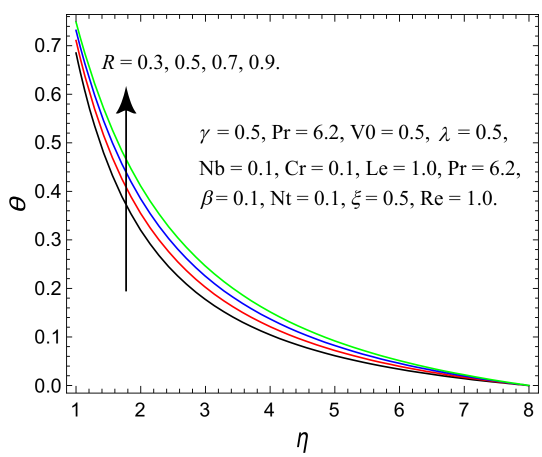

Fig. 16 The influence of (R) on θ

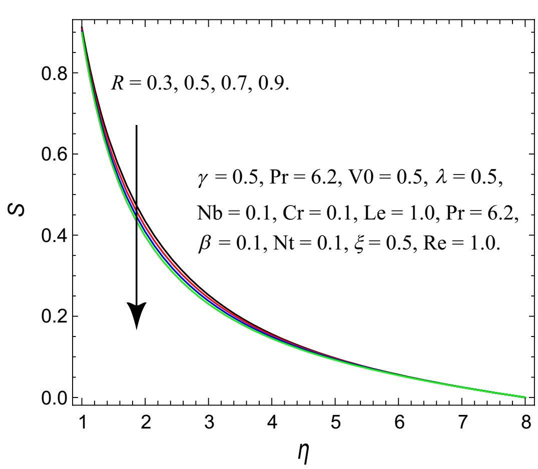

Fig. 17 The influence of (R) on S

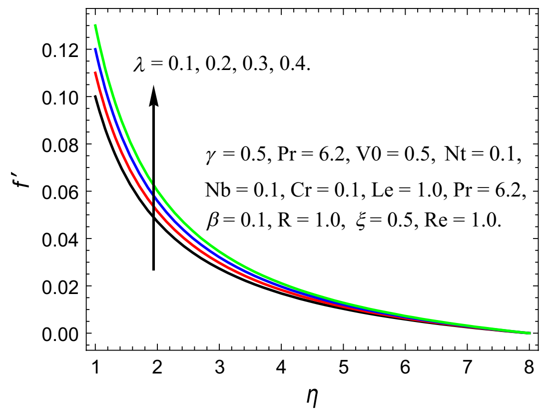

Fig. 18 The Effect of (λ) on f'

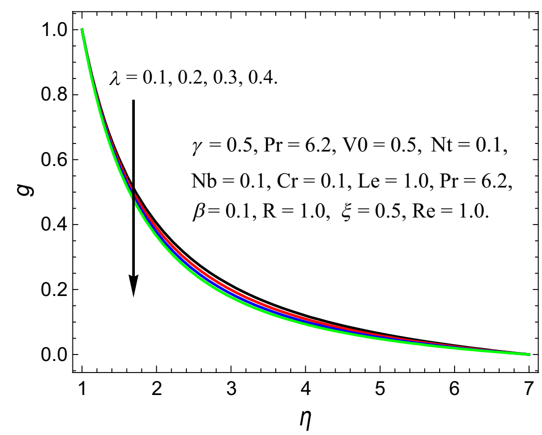

Fig. 19 The influence of (λ) on g

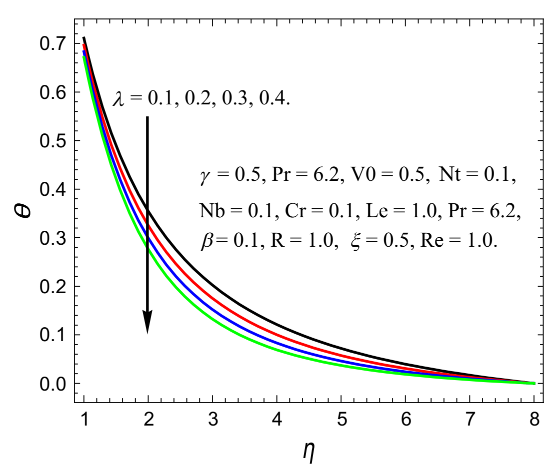

Fig. 20 The influence of (λ) on θ

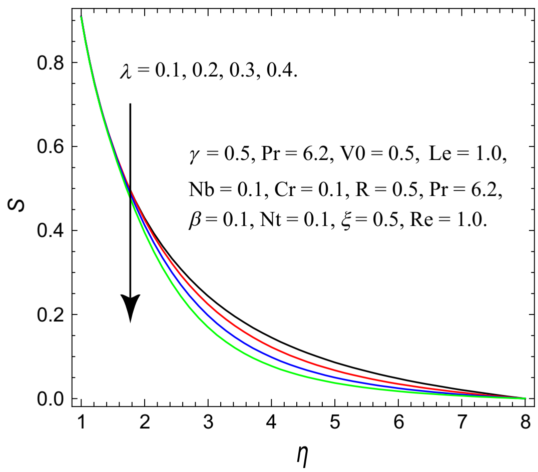

Fig. 21 The influence of (λ) on S

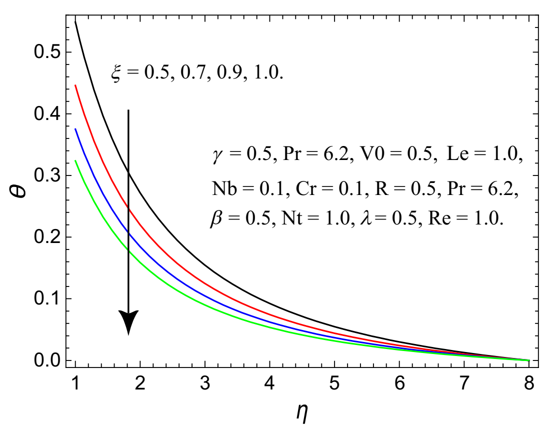

Fig. 22 The influence of (ξ) on θ

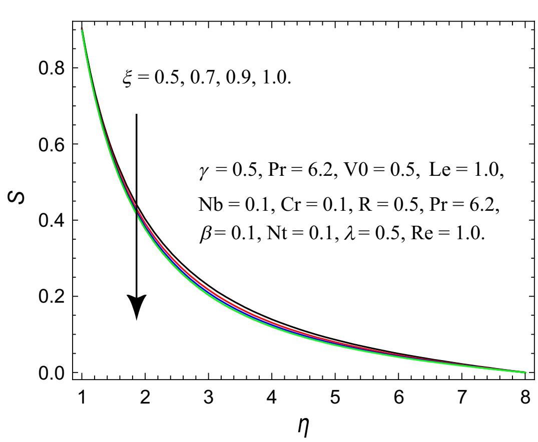

Fig. 23 The influence of (ξ) on S

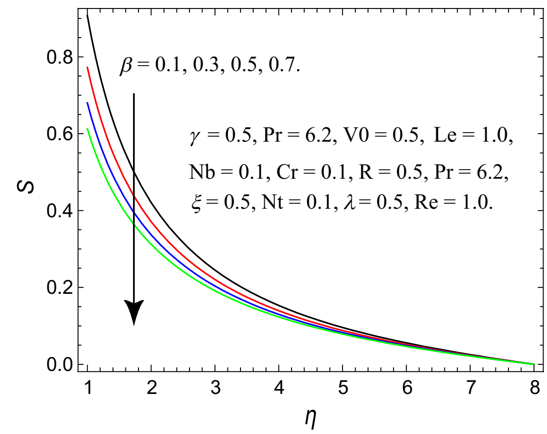

Fig. 24 The influence of (β) on S

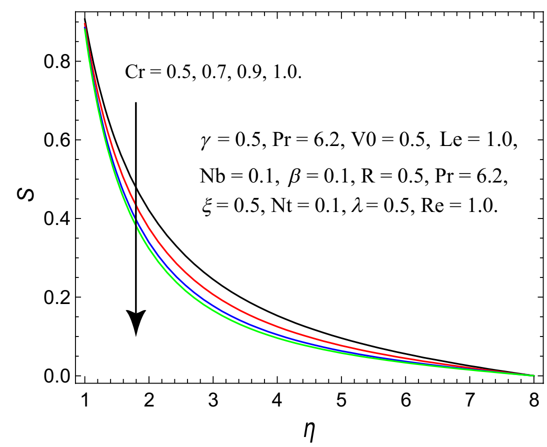

Fig. 25 The influence of (Cr) on S

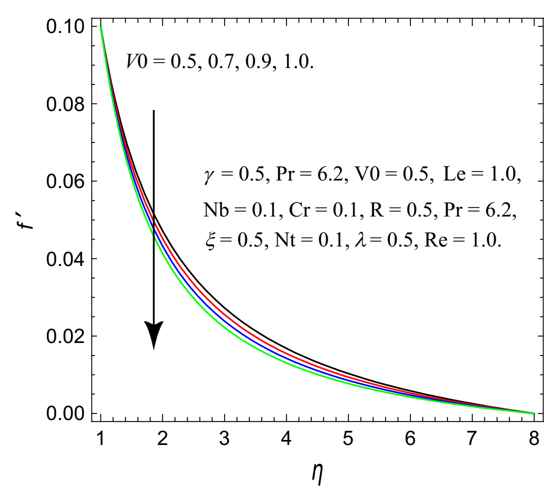

Fig. 26 The influence of ($V0$) on f'\

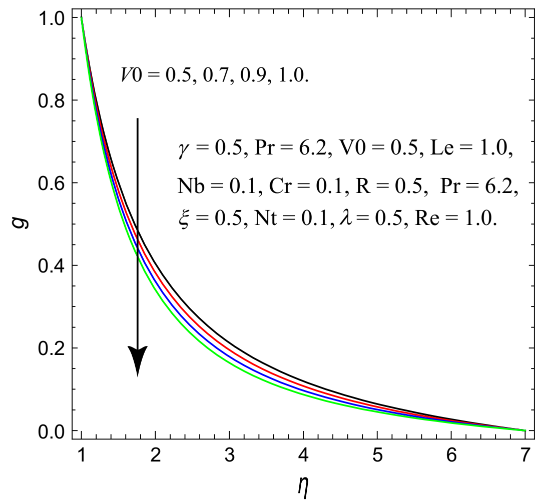

Fig. 27 The influence of $(V0)$ on g

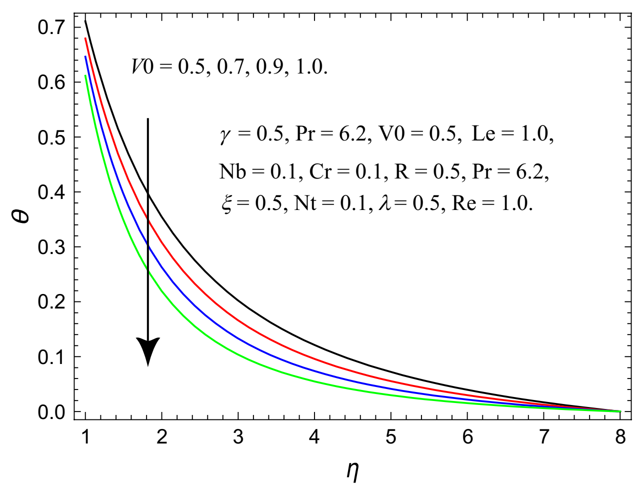

Fig. 28 The influence of $(V0)$ on θ

Conclusions

The consequence of velocity, thermal, concentration slip effects and thermal radiation effects on Buongiorno's mathematical model of nanofluid flow over a swirling cylinder has been considered in this study at the boundary with Cattaneo–Christov model. An efficient FEM analysis is applied to solve the resultant ordinary differential equations and the scatterings of velocity, temperature and concentration are illustrated through graphs. The imperative results of the problem are as follows:

1. Skin friction coefficient, Nusselt number and Sherwood number diminish in the rising values of (Nt), whereas it boosted with increment in (Re).
2. Values of skin friction coefficient and Sherwood number reduce with thermal relaxation parameter (γ). But the Nusselt number escalates with intensify values of (γ).
3. It is professed that temperature and concentration sketches depreciate with step up values of velocity slip temperature (λ), however, the swirling velocity sketches accumulated as values of (λ) rises.
4. It was found that as the values of (V0) develops led to Swirling velocity, radial velocity and temperature sketches diminishes.
5. With optimizing values of (β) and (Cr) concentration sketches shrinks in the entire fluid regime.

Reference

1. Choi SUS, Zhang ZG, Yu W, Lockwood FE, Grulke EA. Anomalous thermal conductivity enhancement in nano-tube suspensions. Appl Phys. 2001;79:2252–4.
2. Ghalambaz M, Doostani A, Chamkha AJ, Ismael MA. Melting of nanoparticles-enhanced phase-change materials in an enclosure: effect of hybrid nanoparticles. Int J Mech Sci. 2017;134:85–97.
3. Sudarsana Reddy P, Chamkha AJ. Heat and mass transfer characteristics of Al_2O_3-water and Ag-water nanofluid through porous media over a vertical cone with heat generation/absorption. J Porous Media. 2017;20:1–17.
4. Sheremet MA, Pop I, Rosca AV. The influence of thermal radiation on unsteady free convection in inclined enclosures filled by a nanofluid with sinusoidal boundary conditions. Int J Numer Methods Heat Fluid Flow. 2018;28(8):1738–53.
5. Munawar S, Saleem N, Mehmood A. Entropy production in the flow over a swirling stretchable cylinder. Thermophys Aeromechanics. 2016;23(3):435–44. https://doi.org/10.1134/s0869864316030136.
6. Deylami HM, Amanifard N, Hosseininezhad SS, Dolati F. Numerical investigation of the wake flow control past a circular cylinder with electro-hydrodynamic actuator. Eur J Mech B Fluids. 2017;66:71–80.
7. Sheikholeslami M. Influence of lorentz forces on nanofluid flow in a porous cylinder considering darcy model. J Mol Liq. 2017;225:903–12.
8. Sheikholeslami M. Magnetic field influence on nanofluid thermal radiation in a cavity with tilted elliptic inner cylinder. J Mol Liq. 2017;229:137–47.
9. Selimefendigil F, Ismael MA, Chamkha AJ. Mixed convection in superposed nanofluid and porous layers in square enclosure with inner rotating cylinder. Int J Mech Sci. 2017;124–125:95–108.
10. Akar S, Rashidi S, Esfahani JA. Second law of thermodynamic analysis for nanofluid turbulent flow around a rotating cylinder. J Therm Anal Calorim. 2017;132(2):1189–200.
11. Azam M, Khan M, Alshomrani AS. Unsteady radiative stagnation point flow of MHD carreau nanofluid over expanding/contracting cylinder. Int J Mech Sci. 2017;130:64–73.
12. Dinarvand S, Hosseini R, Pop I. Axisymmetric mixed convective stagnation-point flow of a nanofluid over a vertical permeable cylinder by tiwari-das nanofluid model. Powder Technol. 2017;311:147–56.
13. Nourazar SS, Hatami M, Ganji DD, Khazayinejad M. Thermal-flow boundary layer analysis of nanofluid over a porous stretching cylinder under the magnetic field effect. Powder Technol. 2017;317:310–9.

14. Hayat T, Khan MI, Waqas M, Alsaedi A. Newtonian heating effect in nanofluid flow by a permeable cylinder. Results Phys. 2017;7:256–62.
15. Hussain A, Malik MY, Salahuddin T, Bilal S, Awais M. Combined effects of viscous dissipation and Joule heating on MHD sisko nanofluid over a stretching cylinder. J Mol Liq. 2017;231:341–52.
16. Zeeshan A, Maskeen MM, Mehmood OU. Hydromagnetic nanofluid flow past a stretching cylinder embedded in non-darcian forchheimer porous media. Neural Comput Appl. 2017;30(11):3479–89.
17. Ramzan M, Sheikholeslami M, Chung JD, Shafee A. Melting heat transfer and entropy optimization owing to carbon nanotubes suspended Casson nanoliquid flow past a swirling cylinder-a numerical treatment. AIP Adv. 2018;8(11):115130. https://doi.org/10.1063/1.5064389.
18. Javed MF, Khan MI, Khan NB, Muhammad R, Rehman MU, Khan SW, Khan TA. Axisymmetric flow of casson fluid by a swirling cylinder. Results Phys. 2018;9:1250–5.
19. Dogonchi AS, Sheremet MA, Ganji DD, Pop I. Free convection of copper – water nanofluid in a porous gap between hot rectangular cylinder and cold circular cylinder under the effect of inclined magnetic field. J Therm Anal Calorim. 2018;135(2):1171–84.
20. Usman M, Soomro FA, Ul Haq R, Wang W, Defterli O. Thermal and velocity slip effects on casson nanofluid flow over an inclined permeable stretching cylinder via collocation method. Int J Heat Mass Transf. 2018;122:1255–63.
21. Karbasifar B, Akbari M, Toghraie D. Mixed convection of Water-Aluminum oxide nanofluid in an inclined lid-driven cavity containing a hot elliptical centric cylinder. Int J Heat Mass Transf. 2018;116:1237–49.
22. Dogonchi AS, Sheremet MA, Pop I, Ganji DD. MHD natural convection of Cu/H2O nanofluid in a horizontal semi-cylinder with a local triangular heater. Int J Numer Methods Heat Fluid Flow. 2018;28(12):2979–96.
23. Nagendramma V, Leelarathnam A, Raju CSK, Shehzad SA, Hussain T. Doubly stratified MHD tangent hyperbolic nanofluid flow due to permeable stretched cylinder. Results Phys. 2018;9:23–32.
24. Abbas N, Saleem S, Nadeem S, Alderremy AA, Khan AU. On stagnation point flow of a micro polar nanofluid past a circular cylinder with velocity and thermal slip. Results Phys. 2018;9:1224–32.
25. Yousefi M, Dinarvand S, Eftekhari Yazdi M, Pop I. Stagnation-point flow of an aqueous titania - copper hybrid nanofluid toward a wavy cylinder. Int J Numer Meth Heat Fluid Flow. 2018;28(7):1716–35.
26. Selimefendigil F, Öztop HF. Analysis and predictive modeling of nanofluid-jet impingement cooling of an isothermal surface under the influence of a rotating cylinder. Int J Heat Mass Transf. 2018;121:233–45.
27. Shirazi M, Shateri A, Bayareh M. Numerical investigation of mixed convection heat transfer of a nanofluid in a circular enclosure with a rotating inner cylinder. J Therm Anal Calorim. 2018;133(2):1061–73.
28. Alizadeh R, Karimi N, Arjmandzadeh R, Mehdizadeh A. Mixed convection and thermodynamic irreversibilities in MHD nanofluid stagnation-point flows over a cylinder embedded in porous media. J Therm Anal Calorim. 2018;135(1):489–506.
29. Rosca NC, Rosca AV, Pop I, Merkin JH. Nanofluid flow by a permeable stretching/shrinking cylinder. Heat Mass Transf. 2019. https://doi.org/10.1007/s00231-019-02730-x.
30. Alsabery AI, Sheremet MA, Chamkha AJ, Hashim I. Impact of nonhomogeneous nanofluid model on transient mixed convection in a double lid-driven wavy cavity involving solid circular cylinder. Int J Mech Sci. 2019;150:637–55.
31. DogonchiHashim AS. Heat transfer by natural convection of Fe3O4-water nanofluid in an annulus between a wavy circular cylinder and a rhombus. Int J Heat Mass Transf. 2019;130:320–32.
32. Mehryan SAM, Izadpanahi E, Ghalambaz M, Chamkha AJ. Mixed convection flow caused by an oscillating cylinder in a square cavity filled with Cu–Al2O3/water hybrid nanofluid. J Therm Anal Calorim. 2019;137(3):965–82.
33. Shehzad SA, Khan SU, Abbas Z, Rauf A. A revised Cattaneo-Christov micropolar viscoelastic nanofluid model with combined porosity and magnetic effects. Appl Math Mech. 2019;41(3):521–32.
34. Raju CSK, Sanjeevi P, Raju MC, Ibrahim SM, Lorenzini G, Lorenzini E. The flow of magnetohydrodynamic Maxwell nanofluid over a cylinder with Cattaneo-Christov heat flux model. Contin Mech Thermodyn. 2017;29(6):1347–63.
35. Dogonchi AS, Chamkha AJ, Seyyedi SM, Ganji DD. Radiative nanofluid flow and heat transfer between parallel disks with penetrable and stretchable walls considering Cattaneo-Christov heat flux model. Heat Transfer-Asian Res. 2018;47(5):735–53.
36. Rauf A, Shehzad SA, Abbas Z, Hayat T. Unsteady three-dimensional MHD flow of the micropolar fluid over an oscillatory disk with Cattaneo-Christov double diffusion. Appl Math Mech. 2019;40(10):1471–86.
37. Li X, Khan AU, Khan MR, Nadeem S, Khan SU. Oblique stagnation point flow of nanofluids over stretching/shrinking sheet with cattaneo-christov heat flux model: existence of dual solution. Symmetry. 2019;11(9):1070.
38. Bhattacharyya A, Seth GS, Kumar R, Chamkha AJ. Simulation of Cattaneo-Christov heat flux on the flow of single and multi-walled carbon nanotubes between two stretchable coaxial rotating disks. J Therm Anal Calorim. 2019. https://doi.org/10.1007/s10973-019-08644-4.
39. Kumar KG, Reddy MG, Sudharani MVVNL, Shehzad SA, Chamkha AJ. Cattaneo-Christov heat diffusion phenomenon in Reiner-Philippoff fluid through a transverse magnetic field. Phys A. 2020;541:123330.
40. Shehzad SA, Reddy MG, Rauf A, Abbas Z. Bioconvection of Maxwell nanofluid under the influence of double diffusive Cattaneo-Christov theories over isolated rotating disk. Phys Scr. 2020;95(4):045207.
41. Rashad AM. Impact of thermal radiation on MHD slip flow of a ferrofluid over a non-isothermal wedge. J Magn Magn Mater. 2017;422:25–31.
42. Rashad A. Unsteady nanofluid flow over an inclined stretching surface with convective boundary condition and anisotropic slip impact. Int J Heat Technol. 2017;35(1):82–90.
43. Ganesh Kumar K, Ramesh GK, Gireesha BJ, Rashad AM. On stretched magnetic flow of carreau nanofluid with slip effects and nonlinear thermal radiation. Nonlinear Eng. 2019;8(1):340–9.
44. El-Kabeir SMM, El-Zahar ER, Modather M, Gorla RSR, Rashad AM. Unsteady MHD slip flow of a ferrofluid over an impulsively stretched vertical surface. AIP Adv. 2019;9(4):045112.
45. Subbarayudu K, Suneetha S, Bala Anki Reddy P, Rashad AM. Framing the activation energy and binary chemical reaction on CNT's with Cattaneo-Christov heat diffusion on maxwell nanofluid in the presence of nonlinear thermal radiation. Arab J Sci Eng. 2019;44(12):10313–25.
46. El-Zahar ER, Rashad AM, Seddek LF. The impact of sinusoidal surface temperature on the natural convective flow of a ferrofluid along a vertical plate. Mathematics. 2019;7(11):1014.
47. Alwawi FA, Alkasasbeh HT, Rashad AM, Idris R. MHD natural convection of sodium alginate casson nanofluid over a solid sphere. Results Phys. 2020;16:102818.
48. Nabwey HA, Khan WA, Rashad AM. Lie group analysis of unsteady flow of kerosene/cobalt ferrofluid past a radiated

stretching surface with navier slip and convective heating. Mathematics. 2020;8(5):826.
49. Reddy SRR, Bala Anki Reddy P, Rashad AM. Activation energy impact on chemically reacting eyring-powell nanofluid flow over a stretching cylinder. Arab J Sci Eng. 2020;45(7):5227–42.
50. Khan WA, Rashad AM, El-Kabeir SMM, El-Hakiem AMA. Framing the MHD micropolar-nanofluid flow in natural convection heat transfer over a radiative truncated cone. Processes. 2020;8(4):379.
51. Ullah Z, Ashraf M, Rashad AM. Magneto-thermo analysis of oscillatory flow around a non-conducting horizontal circular cylinder. J Therm Anal Calorim. 2020;142(4):1567–78.
52. Alwawi FA, Alkasasbeh HT, Rashad A, Idris R. Heat transfer analysis of ethylene glycol-based casson nanofluid around a horizontal circular cylinder with MHD effect. Proc Inst Mech Eng Part C J Mech Eng Sci. 2020;234(13):2569–80.
53. Reddy S, Reddy PBA, Rashad A. Effectiveness of binary chemical reaction on magneto-fluid flow with Cattaneo-Christov heat flux model. Proc Inst Mech Eng Part C J Mech Eng Sci. 2020. https://doi.org/10.1177/0954406220950347.
54. Ghalambaz M, Mehryan SAM, Hajjar A, Veismoradi A. Unsteady natural convection flow of a suspension comprising nano-encapsulated phase change materials (NEPCMs) in a porous medium. Adv Powder Technol. 2020;31(3):954–66.
55. Ghalambaz M, Mehryan SAM, Mozaffari M, Hashem Zadeh SM, Saffari Pour M. Study of thermal and hydrodynamic characteristics of water-nano-encapsulated phase change particles suspension in an annulus of a porous eccentric horizontal cylinder. Int J Heat Mass Transf. 2020;156:119792.
56. Mehryan SAM, Ghalambaz M, Sasani Gargari L, Hajjar A, Sheremet M. Natural convection flow of a suspension containing nano-encapsulated phase change particles in an eccentric annulus. J Energy Storage. 2020;28:101236.
57. Ghalambaz M, Hashem Zadeh SM, Mehryan SAM, Pop I, Wen D. Analysis of melting behavior of PCMs in a cavity subject to a non-uniform magnetic field using a moving grid technique. Appl Math Model. 2020;77:1936–53.
58. Alsabery AI, Hashim I, Hajjar A, Ghalambaz M, Nadeem S, Saffari Pour M. Entropy generation and natural convection flow of hybrid nanofluids in a partially divided wavy cavity including solid blocks. Energies. 2020;13(11):2942.
59. Sudarsan Reddy P, Prasada Rao DRV. Thermo-diffusion and diffusion–thermo effects on convective heat and mass transfer through a porous medium in a circular cylindrical annulus with quadratic density temperature variation–finite element study. J Appl Fluid Mech. 2012;5:139–44.
60. Sreedevi P, Sudarsana Reddy P, Chamkha AJ. Heat and mass transfer analysis of nanofluid over linear and non- linear stretching surface with thermal radiation and chemical reaction. Powder Technol. 2017;315:194–204.
61. Jyothi K, Sudarsana Reddy P, Suryanarayana Reddy M. Influence of magnetic field and thermal radiation on convective flow of SWCNTs-water and MWCNTs-water nanofluid between rotating stretchable disks with convective boundary conditions. Powder Technol. 2018;331:326–37.
62. Sudarsana Reddy P, Chamkha AJ. Heat and mass transfer characteristics of MHD three-dimensional flow over a stretching sheet filled with water - based Alumina nanofluid. Int J Numer Meth Heat Fluid Flow. 2018;28:532–46.
63. Alebraheem J, Ramzan M. Flow of nanofluid with Cattaneo-Christov heat flux model. Appl Nanosci. 2019. https://doi.org/10.1007/s13204-019-01051-z.